Inorganic Chemistry
ARTICLE
pubs.acs.org/IC

Structural Evolution and Properties of Solid Solutions of Hexagonal $InMnO_3$ and $InGaO_3$

Dmitriy A. Rusakov,[†] Alexei A. Belik,[*,†] Stanislav Kamba,[‡] Maxim Savinov,[‡] Dmitry Nuzhnyy,[‡] Taras Kolodiazhnyi,[§] Kazunari Yamaura,[§] Eiji Takayama-Muromachi,[†,§] Fedir Borodavka,[‡] and Jan Kroupa[‡]

[†]International Center for Materials Nanoarchitectonics (MANA) and [§]Superconducting Materials Center (SMC), National Institute for Materials Science (NIMS), 1-1 Namiki, Tsukuba, Ibaraki 305-0044, Japan

[‡]Institute of Physics ASCR, Na Slovance 2, 18221 Prague 8, Czech Republic

S *Supporting Information*

ABSTRACT: Solid solutions $InMn_{1-x}Ga_xO_3$ ($0 \leq x \leq 1$) have been investigated using magnetic, dielectric, specific heat, differential scanning calorimetry (DSC), and high-temperature powder synchrotron X-ray diffraction (HT-SXRD) measurements. It was found that samples with $0.5 \leq x \leq 1$ crystallize in space group $P6_3/mmc$ with $a \sim 3.32$ Å and $c \sim 11.9$ Å, and samples with $0.0 \leq x \leq 0.4$ crystallize in space group $P6_3cm$ with $a \sim 5.8$ Å and $c \sim 11.6$ Å at room temperature. HT-SXRD data revealed the existence of a $P6_3cm$-to-$P6_3/mmc$ phase transition at about 480 K in $InMn_{0.6}Ga_{0.4}O_3$ and at 950 K in $InMn_{0.7}Ga_{0.3}O_3$. However, no dielectric, phonon, second-harmonic-generation, or DSC anomalies were found to be associated with these phase transitions. The phase transition should be improper ferroelectric from the symmetry point of view, but the above-mentioned experimental facts, together with the absence of ferroelectric hysteresis loops, revealed no evidence for ferroelectricity in the low-temperature $P6_3cm$ structure. We suggest that $InMn_{1-x}Ga_xO_3$ corresponds to a nonferroelectric phase of hexagonal $RMnO_3$ with $P6_3cm$ symmetry. The antiferromagnetic phase-transition temperature decreases from 118 K for $x = 0$ to 105 K for $x = 0.1$ and 73 K for $x = 0.2$, and no long-range magnetic ordering could be found for $x \geq 0.3$. Specific heat anomalies associated with short-range magnetic ordering were observed for $0.0 \leq x \leq 0.5$. $InMn_{1-x}Ga_xO_3$ with small Mn contents ($0.8 \leq x \leq 0.98$) has a bright-blue color.

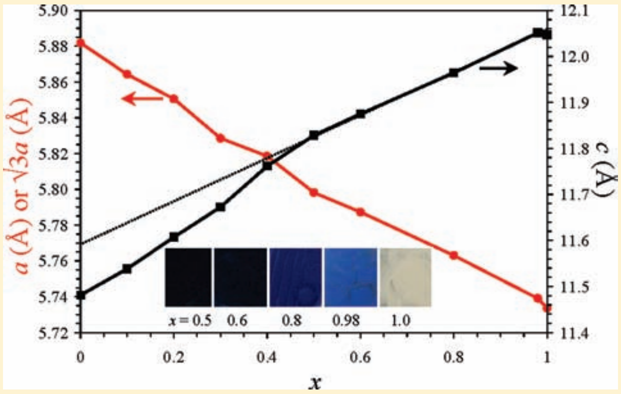

1. INTRODUCTION

Hexagonal manganites $RMnO_3$ (R = Sc, In, Y, and Ho−Lu) crystallize in space group $P6_3cm$ and have a layered structure in which the layers of R^{3+} ions are separated by layers of corner-shared MnO_5 trigonal bipyramids.[1,2] Mn^{3+} ions form a triangular lattice producing strong frustration and resulting in interesting magnetic properties.[3−8] $RMnO_3$ shows antiferromagnetic long-range ordering with Neel temperatures, T_N, of 130 K for $ScMnO_3$ and 70−75 K for $YMnO_3$. $RMnO_3$ also exhibits ferroelectricity with high ferroelectric Curie temperatures (T_{FE}) of 900−1200 K.[1,9−13] Because of the high T_{FE}, an investigation of the ferroelectric−paraelectric phase transition by means of dielectric measurements is difficult because of the increased conductivity. The coexistence of ferroelectricity and magnetism makes $RMnO_3$ a multiferroic material.[14−16]

There are a lot of experimental and theoretical works on hexagonal $RMnO_3$ with R = Sc, Y, and Ho−Lu.[1−22] Several scenarios have been suggested as the origin of the ferroelectric properties of $YMnO_3$: (1) a displacement of the O1−Mn−O2 axis of the MnO_5 polyhedron,[9] (2) an off-centering displacement of Y ions governed by electrostatic and size effects,[14] and (3) an off-centering displacement of Y ions governed by strong hybridization of Y 4d−O 2p bonds.[17−19] Detailed symmetry analyses for $YMnO_3$ show three possible paths from the high-temperature paraelectric $P6_3/mmc$ ($Z = 2$) structure to the low-temperature ferroelectric $P6_3cm$ structure ($Z = 6$), where Z is the number of formula units per unit cell.[9,20,21] Two intermediate phases have been suggested theoretically and experimentally: (1) an intermediate phase with $P6_3/mcm$ ($Z = 6$) symmetry[10,13] and (2) an intermediate nonferroelectric phase with $P6_3cm$ ($Z = 6$) symmetry.[9,14,21] The latest experimental works suggested the hybridization scenario[17−19,21] and the nonferroelectric intermediate phase with $P6_3cm$ symmetry, $P6_3cm \rightarrow P6_3cm \rightarrow P6_3/mmc$ symmetry changes upon heating at $T_{FE} = 920$ K and $T_{npt} = 1258$ K, respectively, where T_{npt} is a phase-transition temperature corresponding to the cell tripling.[21]

$YMnO_3$ is an improper ferroelectric with a polarization value of about 5 $\mu C/cm^2$ along the c axis.[14,20,22] It was suggested that the nonferroelectric $P6_3cm$ phase can be created after the K_3

Received: December 11, 2010
Published: March 18, 2011

dx.doi.org/10.1021/ic102477c | *Inorg. Chem.* 2011, 50, 3559–3566

phonon softening, and subsequently the Γ_1 mode softening induces the ferroelectric $P6_3cm$ phase.[9,14] Fennie and Rabe showed that an improper ferroelectric phase is directly created by K_3 softening.[20] Coupling of the K_3 and Γ_1 modes just significantly enhances polarization. Nevertheless, they also suggested the existence of a paraelectric $P6_3cm$ phase (in an average sense) in an intermediate-temperature range.[20]

Substitution effects on hexagonal $RMnO_3$ (R = Sc, In, Y, and Ho−Lu) have been investigated in a number of papers.[23−33] Magnetocapacitance effects were found in $YMn_{1-x}Ti_xO_3$ solid solutions with a structural phase transition from hexagonal to the $R\bar{3}c$ structure that takes place at around $x = 0.2$.[29,30] A perovskite phase appears in $YMn_{1-x}Fe_xO_3$ solid solutions at around $x = 0.3$.[31] Enhancement of magnetoelectric coupling was observed in $YMn_{1-x}Ga_xO_3$.[27] Because the $YMnO_3$ and $YGaO_3$ ($YInO_3$) end members have the same crystal structure with the $P6_3cm$ space group, hexagonal $YMn_{1-x}Ga_xO_3$ and $YMn_{1-x}In_xO_3$ solid solutions are formed in the whole compositional range.[2,28,32]

$InMnO_3$ belongs to a family of hexagonal manganites, but it has some peculiarities.[34] Its lattice parameters have anomalies compared with other compounds in the series: the a lattice parameter (=5.8758 Å) is smaller than expected, and the c lattice parameter (=11.4715 Å) is larger than expected.[34] $InMnO_3$ has $T_N = 118$ K,[35] and its magnetic structure is different from those of other $RMnO_3$ compounds.[34] It was reported that T_{FE} (=500 K) in $InMnO_3$ is very low compared with other $RMnO_3$ members.[1,36] However, T_{FE} (=500 K) and the ferroelectric properties of $InMnO_3$ have not been recently confirmed.[35] $InGaO_3$ crystallizes in the $P6_3/mmc$ space group and has a structure corresponding to a paraelectric phase of $RMnO_3$ (R = Sc, Y, In, and Ho−Lu).[37] Therefore, by studying the solid solution of $InMn_{1-x}Ga_xO_3$ as a function of the composition, x, one can expect to decrease the temperature of a structural (and possible ferroelectric) phase transition from the $P6_3/mmc$ to $P6_3cm$ space group.

In this work, we report on the preparation of hexagonal solid solutions of $InMn_{1-x}Ga_xO_3$ using a high-pressure technique and their magnetic, dielectric, specific heat, differential scanning calorimetry (DSC), and high-temperature powder synchrotron X-ray diffraction (HT-SXRD) studies. We indeed found that samples with $0.0 \le x \le 0.4$ crystallize in the $P6_3cm$ space group with $a \sim 5.8$ Å and $c \sim 11.6$ Å and samples with $0.5 \le x \le 1$ crystallize in the $P6_3/mmc$ space group with $a \sim 3.32$ Å and $c \sim 11.9$ Å. HT-SXRD data revealed the existence of the $P6_3cm$-to-$P6_3/mmc$ phase transition at about 480 and 950 K in $InMn_{0.6}Ga_{0.4}O_3$ and $InMn_{0.7}Ga_{0.3}O_3$, respectively. However, no dielectric anomalies were found in the megahertz and terahertz frequency ranges, indicating that this transition does not have a ferroelectric origin.

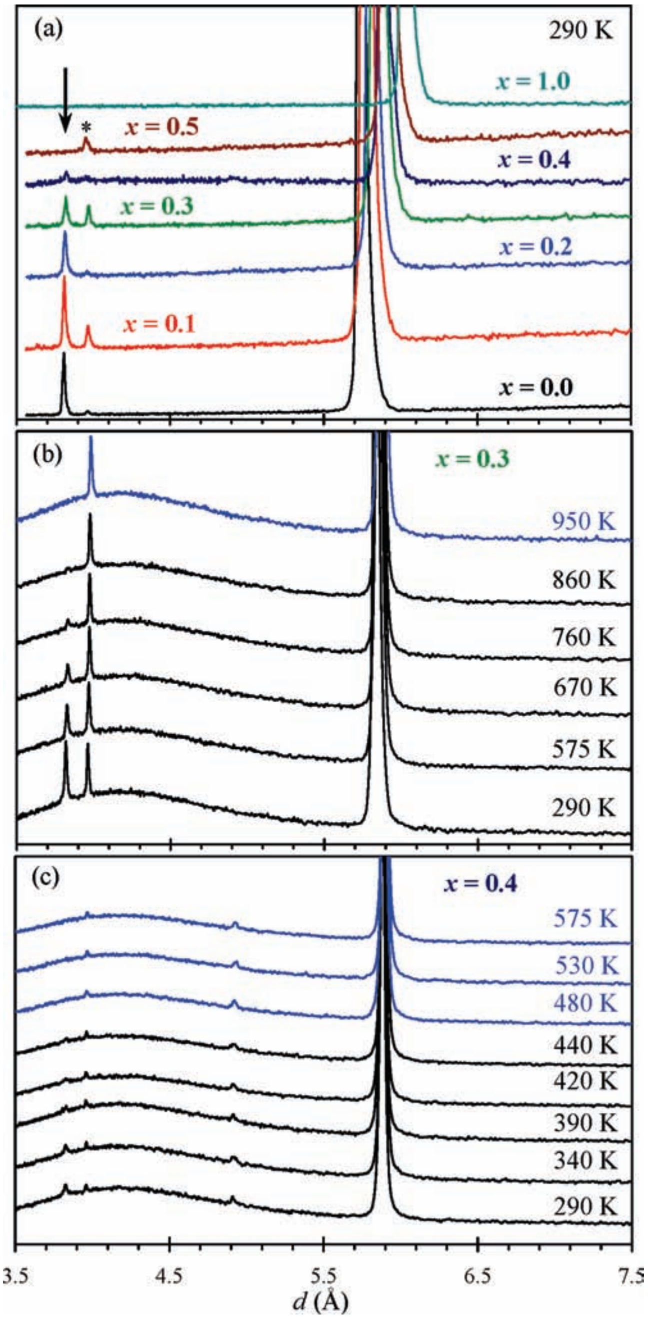

Figure 1. Fragments of powder XRD data. (a) Compositional dependence in $InMn_{1-x}Ga_xO_3$ (measured with Cu Kα radiation at RT). The arrow shows the 102 reflection corresponding to the $(3)^{1/2} \times (3)^{1/2}$ superstructure. The asterisk shows the impurity reflection of In_2O_3 (corundum-type). (b) Temperature dependence in $InMn_{0.7}Ga_{0.3}O_3$ (synchrotron radiation with $\lambda = 0.7741$ Å). (c) Temperature dependence in $InMn_{0.6}Ga_{0.4}O_3$ (synchrotron radiation with $\lambda = 0.7741$ Å).

2. EXPERIMENTAL SECTION

Stoichiometric mixtures of In_2O_3 (99.9%), Ga_2O_3 (99.99%), and Mn_2O_3 were placed in gold capsules and treated at 6 GPa in a belt-type high-pressure apparatus at 1373 K for 30 min (the heating rate was about 110 K/min). After heat treatment, the samples were quenched to room temperature (RT), and the pressure was slowly released. The resultant samples were dense pellets whose color changed from black for $0 \le x \le 0.5$ to blue for $0.8 \le x \le 0.98$ to white for $x = 1$. Because commercial Mn_2O_3 samples often contain impurities of other manganese oxides, we used a homemade single-phase Mn_2O_3, which was prepared from commercial MnO_2 (99.99%) by heating in air at 923 K for 24 h. $InMn_{1-x}Ga_xO_3$ ($0 \le x \le 0.98$) contained small amounts of In_2O_3 and/or InOOH impurities. Single-phase $InCu_{2/3}V_{1/3}O_3$ (crystallizing in space group $P6_3/mmc$)[38] was prepared from In_2O_3, CuO, and V_2O_5 at the same conditions as $InMn_{1-x}Ga_xO_3$. $InCu_{2/3}V_{1/3}O_3$ was used for estimation of the magnetic part of the specific heat of $InMn_{1-x}Ga_xO_3$.

Powder X-ray diffraction (XRD) data were collected at RT on a Rigaku Ultima III diffractometer using Cu Kα radiation (2θ range of 5−100°, a step width of 0.02°, and a counting time of 2−10 s/step). SXRD data were collected at RT on a large Debye−Scherrer camera at the

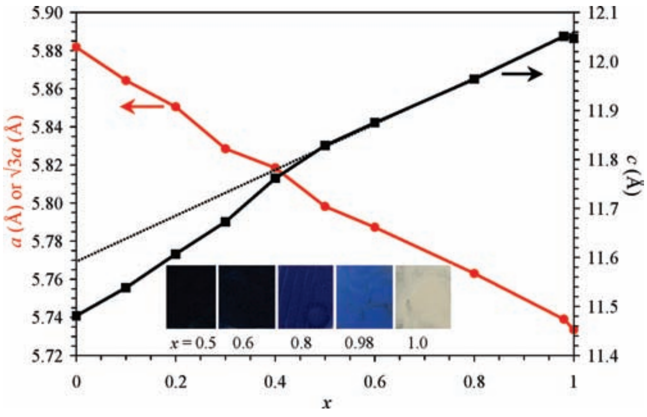

Figure 2. Compositional dependence of the lattice parameters in $InMn_{1-x}Ga_xO_3$ (a and c for $0.0 \leq x \leq 0.4$ and $a(3)^{1/2}$ and c for $0.5 \leq x \leq 1.0$). Insets show colors of $InMn_{1-x}Ga_xO_3$ for $x = 0.5$, 0.6, 0.8. 0.98, and 1.

BL02B2 beamline of SPring-8.[39] The incident beam from a bending magnet was monochromatized to $\lambda \approx 0.423$ Å. The samples were contained in (boro)glass capillary tubes with an inner diameter of 0.2 mm, and the capillary tubes were rotated during measurements. The SXRD data were collected in a 2θ range from 2° to 75° with a step interval of 0.01° (the data from 2.5° to 52.5° were used in the refinements). HT-SXRD data of $InMn_{0.6}Ga_{0.4}O_3$ and $InMn_{0.7}Ga_{0.3}O_3$ were collected at the BL02B2 beamline with $\lambda = 0.7741$ Å in quartz capillary tubes. The XRD data were analyzed by the Rietveld method with *RIETAN-2000*.[40]

Direct-current magnetic susceptibilities, $\chi = M/H$, were measured on a SQUID magnetometer (Quantum Design, MPMS) between 2 and 400 K in applied fields of 0.01, 1, and 5 T under both zero-field-cooled and field-cooled (FC; on cooling) conditions. The specific heat, C_p, was measured from 300 to 2 K at zero magnetic field by a pulse relaxation method using a commercial calorimeter (Quantum Design, PPMS).

For the time-domain terahertz (THz) transmission experiments, we used a Ti:sapphire femtosecond laser oscillator. Linearly polarized THz probing pulses were generated by an interdigitated photoconducting switch from GaAs and detected using the electrooptic sampling with a 1-mm-thick [110] ZnTe crystal. The complex dielectric spectra were taken in the range of 8–55 cm^{-1} (240 GHz to 1.65 THz). Samples were measured in a high-temperature cell (SPECAC P/N 5850) at temperatures from 300 to 900 K. Measurements in the THz region were performed to eliminate conductivity effects, which result in giant values of low-frequency permittivity ($\varepsilon = 15$ in a THz region versus $\varepsilon = 10^3$ in a kHz region). Low-frequency (100 Hz to 1 MHz) dielectric measurements were performed between 300 and 700 K using an HP 4192A impedance analyzer and between 10 and 300 K using an Agilent E4980A LCR meter. For high-temperature Raman studies, a Renishaw RM 1000 Micro-Raman spectrometer equipped with a CCD detector and a Linkam THMS 600 temperature cell was used.

DSC curves were recorded on a Mettler Toledo DSC1 STAR^e system at a heating/cooling rate of 10 K/min under a N_2 flow from 293 to 970 K in open platinum capsules.

Second harmonic generation (SHG) was studied in the reflection geometry in the temperature range of 300–550 K. A Q-switched neodymium–yttrium–aluminum garnet laser was used as a light source, while an SHG signal at 532 nm was detected using a photomultiplier followed by a boxcar integrator.

3. RESULTS

3.1. Powder XRD of $InMn_{1-x}Ga_xO_3$, Structure Analysis, and Color.

Figure 1a shows fragments of XRD patterns of $InMn_{1-x}Ga_xO_3$ at RT. The intensities of reflections corresponding to the $(3)^{1/2} \times (3)^{1/2}$ superstructure with $a \sim 5.8$ Å (e.g., the 102 reflection) decreased with an increase in the Ga content, and they completely disappeared for $x \geq 0.5$. Figure 2 depicts the compositional dependence of the lattice parameters (a and c for $0.0 \leq x \leq 0.4$ and $a(3)^{1/2}$ and c for $0.5 \leq x \leq 1.0$).

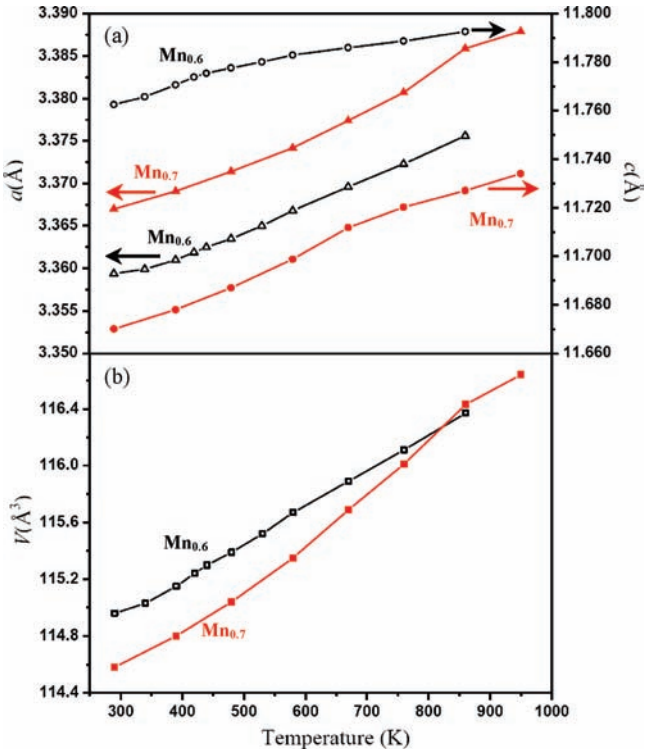

Figure 3. Temperature dependence of (a) the lattice parameters (triangles are a or $a/(3)^{1/2}$; circles are the c parameter) and (b) unit cell volume in $InMn_{0.6}Ga_{0.4}O_3$ (open symbols) and $InMn_{0.7}Ga_{0.3}O_3$ (filled symbols).

Parts b and c of Figure 1 show HT-SXRD data for $InMn_{0.7}Ga_{0.3}O_3$ and $InMn_{0.6}Ga_{0.4}O_3$, respectively. These data show that the intensities of reflections corresponding to $a \sim 5.8$ Å decrease with an increase in the temperature, and completely disappear at 480 and 950 K for $InMn_{0.6}Ga_{0.4}O_3$ and $InMn_{0.7}Ga_{0.3}O_3$, respectively. Figure 3 depicts the temperature dependence of the lattice parameters ($a/(3)^{1/2}$ and c for the $P6_3cm$ structure and a and c for the $P6_3/mmc$ structure) and the unit cell volume ($V/3$ for the $P6_3cm$ structure and V for the $P6_3/mmc$ structure) for $InMn_{0.7}Ga_{0.3}O_3$ and $InMn_{0.6}Ga_{0.4}O_3$.

The crystal structure of $InMn_{0.6}Ga_{0.4}O_3$ at RT was refined in space group $P6_3cm$ using the fractional coordinates of $InMnO_3$ as the initial ones.[34] The crystal structures of $InMn_{0.5}Ga_{0.5}O_3$ at RT and $InMn_{0.6}Ga_{0.4}O_3$ at 660 K were refined in space group $P6_3/mmc$ using the fractional coordinates of $InGaO_3$ as the initial ones.[37] The final lattice parameters, R factors, fractional coordinates, and B parameters are listed in Table 1. Figure 4 displays the observed, calculated, and difference SXRD patterns of $InMn_{0.5}Ga_{0.5}O_3$ at RT as an example.

The polarization, P_S, calculated from the refined structural parameters (see an equation in ref 21) is 9.4 $\mu C/cm^2$ in $InMnO_3$,[34] 13.8 $\mu C/cm^2$ in $InMn_{0.7}Ga_{0.3}O_3$, and 11.6 $\mu C/cm^2$ in $InMn_{0.6}Ga_{0.4}O_3$. Indium atoms are displaced by about 0.1–0.2 Å from their ideal positions of the centrosymmetric $P6_3/mcm$ structure. The similar displacements are found in other

Table 1. Structure Parameters of $InMn_{0.6}Ga_{0.4}O_3$ and $InMn_{0.5}Ga_{0.5}O_3$[a]

site	Wyckoff position	g	x	y	z	B_{iso} (Å^2)
			$InMn_{0.6}Ga_{0.4}O_3$ at 293 K			
In1	2a	1	0	0	0.2539(5)	2.15(9)
In2	4b	1	$1/3$	$2/3$	0.2387(4)	0.12(2)
Mn	6c	0.6	0.3329(12)	0	0	0.21(2)
Ga	6c	0.4	0.3329(12)	0	0	0.21(2)
O1	6c	1	0.326(5)	0	0.1697(9)	0.20(8)
O2	6c	1	0.655(5)	0	0.3446(9)	0.20(8)
O3	2a	1	0	0	0.482(2)	0.20(8)
O4	4b	1	$1/3$	$2/3$	0.000(2)	0.20(8)
			$InMn_{0.6}Ga_{0.4}O_3$ at 660 K			
In	2a	1	0	0	0	1.268(10)
Mn	2c	0.6	$1/3$	$2/3$	$1/4$	1.010(16)
Ga	2c	0.4	$1/3$	$2/3$	$1/4$	1.010(16)
O1	2b	1	0	0	$1/4$	2.14(7)
O2	4f	1	$1/3$	$2/3$	0.0858(2)	1.58(6)
			$InMn_{0.5}Ga_{0.5}O_3$ at 293 K			
In	2a	1	0	0	0	0.670(15)
Mn	2c	0.5	$1/3$	$2/3$	$1/4$	0.18(2)
Ga	2c	0.5	$1/3$	$2/3$	$1/4$	0.18(2)
O1	2b	1	0	0	$1/4$	1.03(9)
O2	4f	1	$1/3$	$2/3$	0.0876(3)	0.51(7)

[a] $InMn_{0.6}Ga_{0.4}O_3$ at 293 K (λ = 0.4231 Å): space group $P6_3cm$ (No. 185), Z = 6, a = 5.81744(5) Å, c = 11.75963(10) Å, and V = 344.658(5) Å^3; R_{wp} = 1.00%, R_p = 0.69%, R_I = 2.63%, and R_F = 2.06%. A common atomic displacement parameter was refined for the oxygen atoms. g is the occupation factor. P_S = 11.6 μC/cm^2. d(In1−O1) = 2.14(3) Å × 3, d(In1−O2) = 2.27(3) Å × 3, d(In1−O3) = 2.68(3) Å, d(In2−O1) = 2.12(2) Å × 3, d(In2−O2) = 2.28(2) Å × 3, d(In2−O4) = 2.80(2) Å. d(Mn−O2) = 1.829(11) Å, d(Mn−O4) = 1.940(4) Å × 2, d(Mn−O3) = 1.948(8) Å, and d(Mn−O1) = 1.996(10) Å. $InMn_{0.6}Ga_{0.4}O_3$ at 660 K (λ = 0.7741 Å): space group $P6_3/mmc$ (No. 194), Z = 2, a = 3.37040(2) Å, c = 11.78914(7) Å, and V = 115.978(1) Å^3; R_{wp} = 5.15%, R_p = 3.75%, R_I = 1.76%, and R_F = 1.55%. $InMn_{0.5}Ga_{0.5}O_3$ (λ = 0.4233 Å): space group $P6_3/mmc$ (No. 194), Z = 2, a = 3.34887(4) Å, c = 11.82740(15) Å, and V = 114.873(2) Å^3; R_{wp} = 1.12%, R_p = 0.69%, R_I = 2.84%, and R_F = 2.57%. Small R_{wp} and R_p values are artifacts due to the large background at $\lambda \approx$ 0.423 Å.

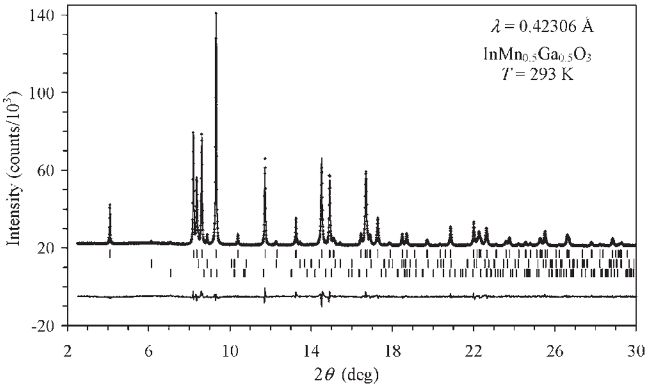

Figure 4. Portions of the observed (crosses), calculated (solid line), and difference powder SXRD patterns of $InMn_{0.5}Ga_{0.5}O_3$ at 293 K. Bragg reflections are indicated by tick marks. The first row is for $InMn_{0.5}Ga_{0.5}O_3$, the second row is for rhombohedral In_2O_3 (2.9 wt %), and the third row is for InOOH (0.3 wt %).

members of the family.[1,13,14] Displacements of indium atoms do not compensate for each other as expected for the K_3 mode distortion.[14]

Refinements of the occupation factor of the Mn/Ga site [together with all other parameters including B(Mn/Ga)] resulted in g(Mn/Ga) = 1.016(2) at RT and g(Mn/Ga) = 1.002(2) at 660 K in $InMn_{0.6}Ga_{0.4}O_3$ and g(Mn/Ga) = 1.031(2) in $InMn_{0.5}Ga_{0.5}O_3$. This fact shows that there are no In^{3+} ions at the Mn/Ga site. Occupation factors of the oxygen sites were checked in $InMn_{0.5}Ga_{0.5}O_3$ at RT [g(O1) = 1.017(5) and g(O2) = 1.017(5)] and in $InMn_{0.6}Ga_{0.4}O_3$ at 660 K [g(O1) = 1.000(5) and g(O2) = 1.008(5)] because the $P6_3/mmc$ structure is simple and has just five refinable (x, y, z, and B) parameters. The g(O) values obtained indicate no oxygen deficiency within the accuracy of the method.

Reflection conditions derived from the indexed reflections afford other possible space groups for $InMn_{1-x}Ga_xO_3$ with $x \leq 0.4$: $P6_3/mcm$ (No. 193), $P\bar{6}c2$ (No. 188), $P\bar{3}c1$ (No. 165), and $P3c1$ (No. 158).[41] We tried these models for analysis of $InMn_{1-x}Ga_xO_3$ ($x \leq 0.4$) in a way similar to the structural analysis of R_2CuTiO_6 (at RT)[42] and $YMnO_3$ (at 1243 K).[21] The $(3)^{1/2} \times (3)^{1/2}$ superstructure reflections of $InMn_{1-x}Ga_xO_3$ ($x \leq 0.4$) could not be fit well with the $P6_3/mcm$ and $P\bar{6}c2$ models, and R values were larger. As the Mn content increases, so does the difference in the R values of the $P6_3cm$ and $P6_3/mcm$ ($P\bar{6}c2$) structural models (see the Supporting Information (SI) for a detailed comparison of R values and fittings for $InMn_{0.7}Ga_{0.3}O_3$ and $InMnO_3$). It is interesting to note that the polar $P6_3cm$ and centrosymmetric $P\bar{3}c1$ models gave almost the same R values (based on powder XRD data) and reasonable structural parameters in the case of $InMnO_3$, $InMn_{1-x}Ga_xO_3$, and $RMnO_3$ (R = Y and Ho−Lu). However, the ferroelectric properties and $P6_3cm$ symmetry of $RMnO_3$ are well established. Therefore, the $P\bar{3}c1$ model can be disregarded.

$InMn_{1-x}Ga_xO_3$ with small Mn contents ($0.8 \leq x \leq 0.98$) has a bright-blue color (Figure 2). This observation is in agreement with the general conclusion of refs 2 and 43 that compounds with Mn^{3+} ions in trigonal-bipyramidal coordination are efficient blue pigments.

3.2. Magnetic Properties of $InMn_{1-x}Ga_xO_3$. Figure 5 shows the total specific heat (C_p) of $InMn_{1-x}Ga_xO_3$ (x = 0, 0.1, and 0.2) and $InCu_{2/3}V_{1/3}O_3$ plotted as C_p/T vs T and the magnetic part of the specific heat (C_m) for $InMn_{1-x}Ga_xO_3$ (x = 0, 0.1, 0.2, 0.3, and 0.4) and $InCu_{2/3}V_{1/3}O_3$ plotted as C_m/T vs T. The lattice contribution (C_L) used in ref 35 for $InMnO_3$ and estimated based on the specific heat of $InGaO_3$ was adopted for all cases to calculate C_m ($C_m = C_p - C_L$). The specific heat data of $InCu_{2/3}V_{1/3}O_3$ were used to justify the validity of our C_L. In ref 35, C_L of $InMnO_3$ was estimated using two Debye functions and one Einstein function. In ref 38, C_L of $InCu_{2/3}V_{1/3}O_3$ was estimated using one Debye function and three Einstein functions and also by the quantum Monte Carlo method. The magnetic entropy of $InCu_{2/3}V_{1/3}O_3$ was almost the same: 3.4 J/(mol K) in ref 38 versus 3.43 J/(mol K) in our present work. Therefore, the estimated C_L can work well for hexagonal $InMO_3$-type compounds. Estimation of the magnetic entropy for $InMn_{1-x}Ga_xO_3$ is given in the SI.

The C_m/T vs T curves demonstrate sharp peaks at 118 K for $InMnO_3$ and at 105 K for $InMn_{0.9}Ga_{0.1}O_3$ due to long-range antiferromagnetic ordering plus broad anomalies at around 50 K.

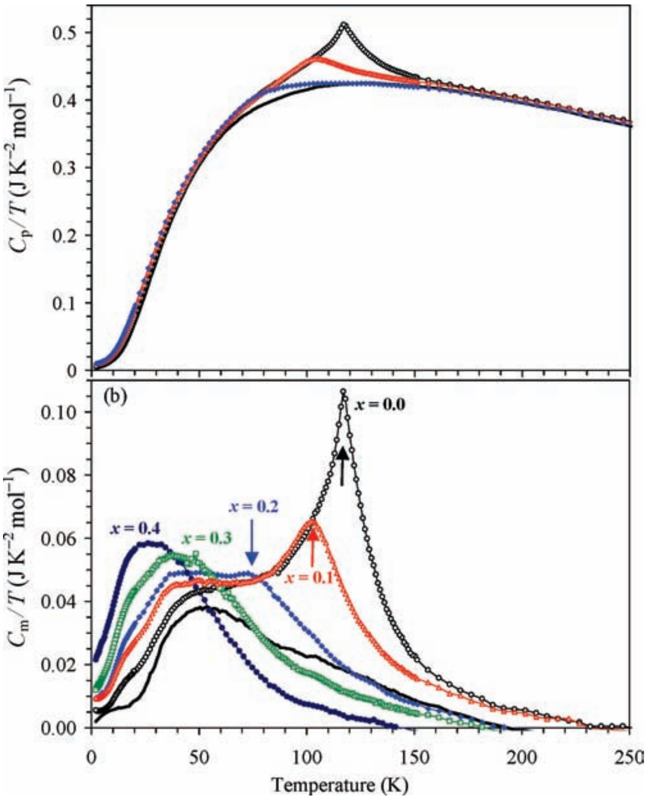

Figure 5. (a) C_p/T vs T curves for $InMn_{1-x}Ga_xO_3$ ($x = 0, 0.1$, and 0.2) (lines with symbols) and $InCu_{2/3}V_{1/3}O_3$ (line). (b) C_m/T vs T curves for $InMn_{1-x}Ga_xO_3$ ($x = 0, 0.1, 0.2, 0.3$, and 0.4) (lines with symbols) and $InCu_{2/3}V_{1/3}O_3$ (line). The arrows also show T_N.

The two-peak features can still be seen for $InMn_{0.8}Ga_{0.2}O_3$ with the first peak at around 70 K. $InMn_{1-x}Ga_xO_3$ with $x \geq 0.3$ shows only a broad anomaly below 50 K.

The inverse magnetic susceptibilities of $InMn_{1-x}Ga_xO_3$ exhibit small drops at T_N for $x = 0, 0.1$, and 0.2 due to a very weak ferromagnetic component (Figure 6). The magnetic susceptibility data in the temperature range of 250−400 K were fit by the simple Curie−Weiss equation

$$\chi(T) = \mu_{\text{eff}}^2 N[3k_B(T-\theta)]^{-1} \qquad (1)$$

where μ_{eff} is the effective magnetic moment, N is Avogadro's number, k_B is Boltzmann's constant, and θ is the Curie−Weiss constant. The experimental effective magnetic moments are very close to the expected value of 4.90 μ_B for Mn^{3+} for all of the samples. The Curie−Weiss constant, which reflects the strength of magnetic interactions, gradually decreases with increasing x. The large $|\theta|$ values indicate that a strong antiferromagnetic interaction between Mn^{3+} ions persists.

3.3. Thermal, Dielectric, and Phonon Properties of $InMn_{1-x}Ga_xO_3$.

No anomalies were found on the DSC curves of $InMn_{1-x}Ga_xO_3$ between 300 and 970 K, and the phase composition of the samples did not change (except for the disappearance of the InOOH impurity, if present). No anomalies were also found in the temperature dependence of the dielectric permittivity measured at 640 GHz (19.2 cm^{-1}) up to 900 K (Figure 7) and at 1 MHz up to 700 K (Figure 8) in $InMn_{0.6}Ga_{0.4}O_3$. The permittivity monotonically increases on heating, whereas a peak in $\varepsilon'(T)$ should be seen at T_{FE} in the THz or MHz frequency range at a displacive or order−disorder phase transition, respectively. Unfortunately, low-frequency intrinsic complex dielectric permittivity above 300 K is screened by extrinsic permittivity coming from the Maxwell−Wagner polarization due to conductivity of the samples. Therefore, the permittivity noticeably increases on heating and reaches values of 10^1−10^4 in $InMn_{1-x}Ga_xO_3$ (Figures 8 and S2 in the SI). The least influence of conductivity on $\varepsilon'(T)$ occurs at the highest frequency; therefore, the 1 MHz permittivity remains smaller than ∼100 in the whole temperature range below 700 K (see Figures 8 and S2 in the SI). In such a case, the order−disorder phase transition should be revealed in $\varepsilon'(T)$ by a strong anomaly, which is not seen in Figure 8. This means that the order−disorder ferroelectric phase transition can be excluded for $InMn_{0.6}Ga_{0.4}O_3$.

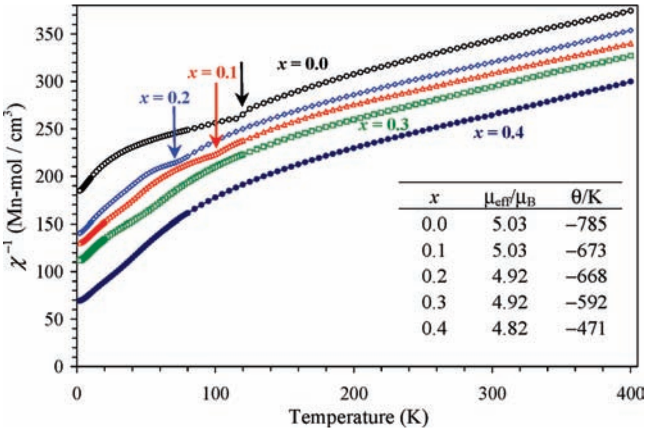

x	μ_{eff}/μ_B	θ/K
0.0	5.03	−785
0.1	5.03	−673
0.2	4.92	−668
0.3	4.92	−592
0.4	4.82	−471

Figure 6. Temperature dependence of the inverse magnetic susceptibilities of $InMn_{1-x}Ga_xO_3$ ($x = 0, 0.1, 0.2, 0.3$, and 0.4) measured at 5 T in the FC mode on cooling. The fitting results with the simple Curie−Weiss equation between 250 and 400 K are given. The arrows show T_N.

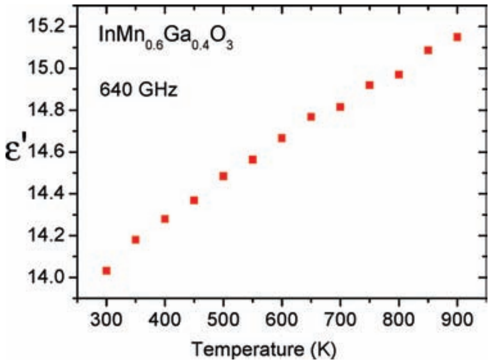

Figure 7. Temperature dependence of permittivity for $InMn_{0.6}Ga_{0.4}O_3$ measured at 640 GHz on heating.

From SXRD data, we know that the tripling of the unit cell occurs on cooling and the structure changes from high-temperature $P6_3/mmc$ symmetry to low-temperature $P6_3cm$ symmetry. In such a case, the phase transition should be an improper ferroelectric (i.e., the order parameter of the phase transition is not a polarization or a polar phonon from the Brillouin zone center but a phonon from the Brillouin zone edge),[9,20,44] and only a small jump in THz of $\varepsilon'(T)$ can be expected at T_{FE}.[44] However, no such jumps were observed. Ferroelectric hysteresis loops should

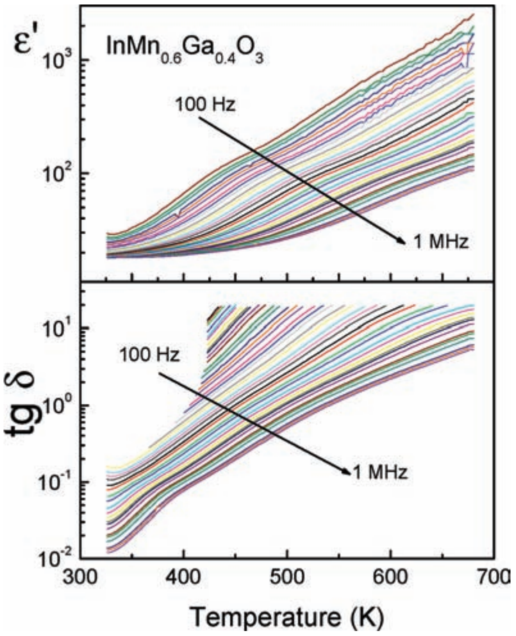

Figure 8. Temperature dependence of (a) permittivity and (b) dielectric loss tan δ for $InMn_{0.6}Ga_{0.4}O_3$ measured at various frequencies between 100 Hz and 1 MHz. Data were taken on cooling.

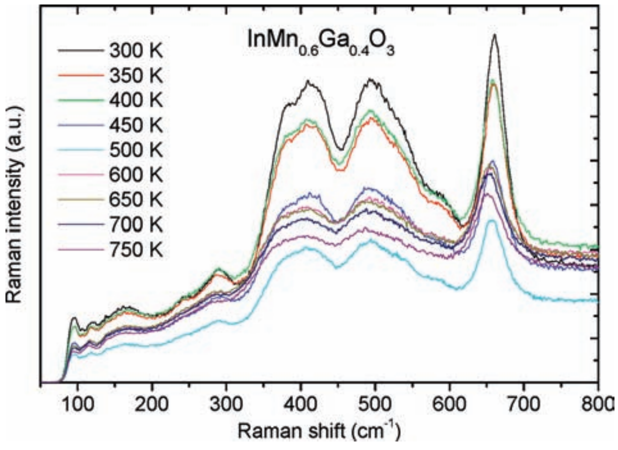

Figure 9. Raman spectra of $InMn_{0.6}Ga_{0.4}O_3$ at different temperatures.

exist in an improper ferroelectric phase. Our measurements performed below RT in $InMn_{0.6}Ga_{0.4}O_3$ (the sample was slightly leaky above RT) did not reveal any ferroelectric hysteresis loops (see Figure S3 in the SI). Only loss dielectric curves were observed. The $P6_3cm$ structure is noncentrosymmetric; therefore, some SHG signals should be generated under illumination of a laser beam. Unfortunately, no SHG signal was observed in $InMn_{0.6}Ga_{0.4}O_3$ up to 550 K. The black color of the samples could significantly reduce the reflected signal. All of the above-mentioned experimental facts give evidence that the $P6_3cm$ phase is either only very slightly ferroelectrically distorted or nonferroelectric.

A structural change should be revealed also in the Raman scattering spectra. Temperature-dependent Raman spectra of $InMn_{0.6}Ga_{0.4}O_3$ are shown in Figure 9. All phonons exhibit a decrease of the intensities on heating presumably because of an increase of phonon damping with temperature. No phonons disappear above 480 K, although the unit cell is 3 times smaller above 480 K and, therefore, the theoretical number of Raman-active modes should reduce from 38 (in $P6_3cm$) to only 5 modes (in $P6_3/mmc$).[45] At least 7 and 8 modes were resolved in our Raman spectra above and below 480 K, respectively. A significantly lower number of modes (than predicted) observed below 480 K is probably due to mode overlapping and high phonon damping.

4. DISCUSSION

On the basis of XRD data, we observed a composition-driven structural transformation from the $P6_3cm$ structure ($Z = 6$) to the $P6_3/mmc$ structure ($Z = 2$) in the solid solutions of $InMn_{1-x}Ga_xO_3$. The $x = 0.3$ and 0.4 samples with the $P6_3cm$ structure near the transformation boundary show similar temperature-driven structural transitions. A linear extrapolation of the phase-transition temperature for $x = 0$ gives about 2000 K for the $P6_3cm$-to-$P6_3/mmc$ transition in $InMnO_3$. This estimation is consistent with the experimental high-temperature structural data for $YMnO_3$ and $YbMnO_3$, where the $P6_3cm$-to-$P6_3/mmc$ transition was detected above 1200 K in $YMnO_3$[11,21] and no transition was found in $YbMnO_3$ up to 1350 K.[11] Other estimations of this phase-transition temperature for $RMnO_3$ (R = Y and Ho−Lu) gave the value of 1430 K.[9]

The compositional dependence of the lattice parameters of $InMn_{1-x}Ga_xO_3$ is similar to that of $YMn_{1-x}Ga_xO_3$;[28] that is, the a parameter decreases and the c parameter increases with increasing x. A different behavior was observed in $YMn_{1-x}In_xO_3$ and $YMn_{1-x}(Cu_{0.5}Ti_{0.5})_xO_3$,[32,46] where both a and c parameters increase with increasing x. The lattice parameters change monotonically in $InMn_{1-x}Ga_xO_3$ without any steplike anomalies near $x = 0.4$−0.5. Therefore, the transition from the $P6_3cm$ structure to the $P6_3/mmc$ structure seems to be smooth (i.e., second order).

As was already mentioned, the $P6_3cm$-to-$P6_3/mmc$ transition in $InMn_{1-x}Ga_xO_3$ is not accompanied by any dielectric anomaly in the THz or radio frequency region (see Figure 7) at critical temperatures, where the phase transitions were revealed in HT-SXRD. Also, no ferroelectric hysteresis loops were observed at low temperatures. This means that these transitions do not have a ferroelectric−paraelectric nature. Both phases seem to be paraelectric. This is consistent with our previous paper claiming that $InMnO_3$ is not ferroelectric.[35]

Crystallization of a compound in a polar crystal class is the necessary but not sufficient condition for the appearance of ferroelectric properties. R_2CuTiO_6 (R = Y, Dy, Ho, Er, and Yb) crystallizes in the hexagonal $P6_3cm$ structure similar to $RMnO_3$;[42] however, as in the case of $InMn_{1-x}Ga_xO_3$, no ferroelectric properties and transitions have also been found.[47,48] The large size difference between Cu^{2+} and Ti^{4+} ions has been suggested as a possible origin of the absence of ferroelectric properties. The similar mechanism may be responsible for the absence of ferroelectric properties in $InMn_{1-x}Ga_xO_3$ because the electronic properties of Mn^{3+} (d^4) and Ga^{3+} (d^{10}) are different. The different electronic properties of Mn^{3+} and Ga^{3+} may result in a short-range local ordering of these ions. The short-range ordering of Cu^{2+} and V^{5+} ions has been observed in $InCu_{2/3}V_{1/3}O_3$.[38] The average structure (determined by XRD) of $InMn_{1-x}Ga_xO_3$ above T_{ntp} is $P6_3/mmc$ but the structure in the local regions may deviate from $P6_3/mmc$, resulting in the observation of a larger number of Raman modes (Figure 9) because Raman spectroscopy is sensitive to local distortions. For example, Raman modes are often observed in pseudocubic perovskites, where all modes should be forbidden.

The paraelectric properties of $InMn_{1-x}Ga_xO_3$ can also be understood in the framework of the hybridization picture proposed as an origin of ferroelectric properties of $YMnO_3$.[17−19,21] It is suggested that the Y1−O3 bond along the polar c axis plays a crucial role.[19] In $YMnO_3$, the Y1−O3 bond length (=2.298 Å) is comparable with other Y1−O bond lengths [d(Y1−O1) = 2.267 Å × 3 and d(Y1−O2) = 2.308 Å × 3].[21] The symmetry of $YMnO_3$ remains the same ($P6_3cm$) above T_{FE} (≈920 K), but the Y1−O3 bond length suddenly increases.[21] In $InMnO_3$, the In1−O3 bond length (=2.41 Å) is noticeably larger than other In1−O bond lengths [d(In1−O1) = 2.15 Å and d(In1−O2) = 2.16 Å].[34] In $InMn_{1-x}Ga_xO_3$, the In1−O3 bond length further increases: d(In1−O1) = 2.18 Å, d(In1−O2) = 2.23 Å, and d(In1−O3) = 2.61 Å in $InMn_{0.7}Ga_{0.3}O_3$ (see the SI) and d(In1−O1) = 2.14 Å, d(In1−O2) = 2.27 Å, and d(In1−O3) = 2.68 Å in $InMn_{0.6}Ga_{0.4}O_3$ (Table 1). Therefore, there should be no In1−O3 hybridization in $InMn_{1-x}Ga_xO_3$.

We note that a recent theoretical study of $InMnO_3$ suggested the existence of the In1−O3 hybridization.[49] However, theoretical calculations were performed using theoretically optimized structural parameters for the ideal $InMnO_3$ at 0 K. The In1−O3 bond length (=2.286 Å) is much shorter in the theoretically optimized structure. The experimental crystal structure of $InMnO_3$ may deviate from the theoretically optimized structure because of some peculiarities of the synthesis. The oxygen loss was detected during the ambient pressure synthesis of $InMnO_3$.[34] This fact may indicate the existence of a small amount of oxygen vacancies, $InMnO_{3-\delta}$. The introduction of oxygen vacancies into hexagonal $YMnO_3$ results in a sudden increase of the Y1−O3 distance up to 2.455 Å in $YMnO_{2.95}$ and 2.589 Å in $YMnO_{2.85}$, and the structure becomes centrosymmetric with $P6_3/mmc$ symmetry at RT in $YMnO_{2.80}$.[50] The c lattice parameter of $YMnO_{3-\delta}$ increases sharply in comparison with that of $YMnO_3$.[50] The anomalously large c parameter was observed in $InMnO_3$ compared with other $RMnO_3$ members.[34] Indium-containing impurities were found in $InMnO_3$ and $InMn_{1-x}Ga_xO_3$ during the high-pressure synthesis.[35] This fact may indicate the existence of a small amount of cation and oxygen vacancies, $In_{1-x}MnO_{3-\delta}$. Indeed, a single-phase sample corresponding to the total composition of $In_{0.9}MnO_{2.85}$ was prepared at high pressure.[51,52] Significant cation and oxygen deficiency can be accommodated in thin films of hexagonal manganites; however, survival of the ferroelectric properties has not been investigated.[53] In the framework of the hybridization picture, $InMn_{1-x}Ga_xO_3$ should correspond to the nonferroelectric phase of $YMnO_3$ with $P6_3cm$ symmetry.

Long-range magnetic ordering survives up to x = 0.2 in $InMn_{1-x}Ga_xO_3$, and T_N decreases with x as expected. Similar trends have been observed in $YMn_{1-x}In_xO_3$ solid solutions.[32] The broad anomaly observed in the C_m/T vs T curves of $InMn_{1-x}Ga_xO_3$ for $x \geq 0.3$ probably originated from the short-range magnetic interactions between Mn^{3+} ions. The large $|\theta|$ values even for the x = 0.3 and 0.4 samples show that antiferromagnetic interactions between Mn^{3+} ions are strong.

THz permittivity values of $InMn_{0.6}Ga_{0.4}O_3$ are in agreement with those of other hexagonal manganites $RMnO_3$ (R = Sc, In, Y, and Lu) measured in the radio frequency range (ε = 15−22 at 150−300 K).[5,35] Very recently, there was a report about THz of $\varepsilon'(T)$ in hexagonal $YMnO_3$. It exhibits an increase of ε' from 12 at 300 K to 17 at 900 K (measured at 19 cm^{-1}).[54] The small increase of ε' at THz with temperature is caused by a slight decrease of several phonon frequencies on heating due to thermal expansion of the crystal lattice.[54]

The permittivity of $InMnO_3$ shows a bump at T_N (ref 35 and Figure S1 in the SI) that is very similar to the anomalies observed in $LuMnO_3$ and $YMnO_3$ at T_N.[5] The decrease of ε' below T_N provides evidence of the spin−phonon coupling in $InMnO_3$. A change of the slope in $\varepsilon'(T)$ near T_N was seen also in $InMn_{1-x}Ga_xO_3$ (x = 0.1 and 0.2; see Figure S1 in the SI), but the change is much smaller than that of $InMnO_3$.. This gives evidence that the spin−phonon coupling reduces with gallium doping similar to $YMn_{1-x}In_xO_3$[32] or $Y_{1-x}Eu_xMnO_3$.[54]

In conclusion, composition- and temperature-driven structural $P6_3cm$-to-$P6_3/mmc$ transitions were found in $InMn_{1-x}Ga_xO_3$. Remarkably, no dielectric, phonon, or DSC anomalies were found to be associated with this phase transition. Both phases seem to be paraelectric. We suggest that $InMn_{1-x}Ga_xO_3$ corresponds to a nonferroelectric phase of hexagonal $RMnO_3$ with $P6_3cm$ symmetry. The antiferromagnetic phase transition temperature decreases from 118 K for x = 0 to 105 K for x = 0.1 and 73 K for x = 0.2, and no long-range magnetic ordering could be found for $x \geq 0.3$. Specific heat anomalies associated with short-range magnetic ordering were observed for $0.0 \leq x \leq 0.5$.

■ ASSOCIATED CONTENT

Supporting Information. Low-frequency, high- and low-temperature dielectric data, polarization hysteresis loops, estimation of the magnetic entropy, Raman spectra of $InMnO_3$, $InMn_{1-x}Ga_xO_3$, $InCu_{2/3}V_{1/3}O_3$, and $InGaO_3$ ceramics, R values and fittings in different structural models, and structural data of $InMn_{0.7}Ga_{0.3}O_3$ at RT in the $P6_3cm$ and $P\bar{3}c1$ models. This material is available free of charge via the Internet at http://pubs.acs.org.

■ AUTHOR INFORMATION

Corresponding Author

*E-mail: Alexei.Belik@nims.go.jp.

■ ACKNOWLEDGMENT

This work was supported by the World Premier International Research Center Initiative on Materials Nanoarchitectonics (MEXT, Japan), by the NIMS Individual-Type Competitive Research Grant, by the Japan Society for the Promotion of Science (JSPS) through its “Funding Program for World-Leading Innovative R&D on Science and Technology (FIRST Program)”, and by a Grant-in-Aid for Scientific Research (Grant 22246083) from JSPS, Japan. The synchrotron radiation experiments were performed at the SPring-8 with the approval of the Japan Synchrotron Radiation Research Institute (Proposals 2009A1136 and 2010A1215). We thank Dr. J. Kim and N. Tsuji for their assistance at SPring-8. Support from the Czech Science Foundation (Projects 202/09/0682 and 202/09/H0041) SVV-2010-261303 and AVOZ10100520 is acknowledged.

■ REFERENCES

(1) Abrahams, S. C. *Acta Crystallogr., Sect. B* **2001**, *57*, 485.

(2) Smith, A. E.; Mizoguchi, H.; Delaney, K.; Spaldin, N. A.; Sleight, A. W.; Subramanian, M. A. *J. Am. Chem. Soc.* **2009**, *131*, 17084.

(3) Munoz, A.; Alonso, J. A.; Martinez-Lope, M. J.; Casais, M. T.; Martinez, J. L.; Fernandez-Diaz, M. T. *Phys. Rev. B* **2000**, *62*, 9498.

(4) Munoz, A.; Alonso, J. A.; Martinez-Lope, M. J.; Casais, M. T.; Martinez, J. L.; Fernandez-Diaz, M. T. *Chem. Mater.* **2001**, *13*, 1497.

(5) Katsufuji, T.; Mori, S.; Masaki, M.; Moritomo, Y.; Yamamoto, N.; Takagi, H. *Phys. Rev. B* **2001**, *64*, 104419.

(6) Tachibana, M.; Yamazaki, J.; Kawaji, H.; Atake, T. *Phys. Rev. B* **2005**, *72*, 064434.

(7) Bieringer, M.; Greedan, J. E. *J. Solid State Chem.* **1999**, *143*, 132.

(8) Fiebig, M.; Frohlich, D.; Kohn, K.; Leute, S.; Lottermoser, T.; Pavlov, V. V.; Pisarev, R. V. *Phys. Rev. Lett.* **2000**, *84*, 5620.

(9) Lonkai, Th.; Tomuta, D. G.; Amann, U.; Ihringer, J.; Hendrikx, R. W. A.; Tobbens, D. M.; Mydosh, J. A. *Phys. Rev. B* **2004**, *69*, 134108.

(10) Nenert, G.; Pollet, M.; Marinel, S.; Blake, G. R.; Meetsma, A.; Palstra, T. T. M. *J. Phys.: Condens. Matter* **2007**, *19*, 466212.

(11) Jeong, I.-K.; Hur, N.; Proffen, Th. *J. Appl. Crystallogr.* **2007**, *40*, 730.

(12) Fujimura, N.; Ishida, T.; Yoshimura, T.; Ito, T. *Appl. Phys. Lett.* **1996**, *69*, 1011.

(13) Abrahams, S. C. *Acta Crystallogr., Sect. B* **2009**, *65*, 450.

(14) Van Aken, B. B.; Palstra, T. T. M.; Filippetti, A.; Spaldin, N. A. *Nat. Mater.* **2004**, *3*, 164.

(15) Ramesh, R.; Spaldin, N. A. *Nat. Mater.* **2007**, *6*, 21.

(16) Lottermoser, T.; Lonkai, T.; Amann, U.; Hohlwein, D.; Ihringer, J.; Fiebig, M. *Nature* **2004**, *430*, 541.

(17) Cho, D.-Y.; Kim, J.-Y.; Park, B.-G.; Rho, K.-J.; Park, J.-H.; Noh, H.-J.; Kim, B. J.; Oh, S.-J.; Park, H.-M.; Ahn, J.-S.; Ishibashi, H.; Cheong, S.-W.; Lee, J. H.; Murugavel, P.; Noh, T. W.; Tanaka, A.; Jo, T. *Phys. Rev. Lett.* **2007**, *98*, 217601.

(18) Zhong, C. G.; Jiang, Q.; Zhang, H.; Jiang, X. F. *Appl. Phys. Lett.* **2009**, *94*, 224107.

(19) Kim, J.; Cho, K. C.; Koo, Y. M.; Hong, K. P.; Shin, N. *Appl. Phys. Lett.* **2009**, *95*, 132901.

(20) Fennie, C. J.; Rabe, K. M. *Phys. Rev. B* **2000**, *72*, 100103(R).

(21) Gibbs, A. S.; Knight, K. S.; Lightfoot, P. *Phys. Rev. B* **2011**, *83*, 094111.

(22) Choi, T.; Horibe, Y.; Yi, H. T.; Choi, Y. J.; Wu, W.; Cheong, S.-W. *Nat. Mater.* **2010**, *9*, 253.

(23) Katsufuji, T.; Masaki, M.; Machida, A.; Moritomo, M.; Kato, K.; Nishibori, E.; Takata, M.; Sakata, M.; Ohoyama, K.; Kitazawa, K.; Takagi, H. *Phys. Rev. B* **2002**, *66*, 134434.

(24) Zhou, H. D.; Lu, J.; Vasic, R.; Vogt, B. W.; Janik, J. A.; Brooks, J. S.; Wiebe, C. R. *Phys. Rev. B* **2007**, *75*, 132406.

(25) Zhou, H. D.; Janik, J. A.; Vogt, B. W.; Jo, Y. J.; Balicas, L.; Case, M. J.; Wiebe, C. R.; Denyszyn, J. C.; Goodenough, J. B.; Cheng, J. G. *Phys. Rev. B* **2006**, *74*, 094426.

(26) Zhou, H. D.; Denyszyn, J. C.; Goodenough, J. B. *Phys. Rev. B* **2007**, *72*, 224401.

(27) Nugroho, A. A.; Bellido, N.; Adem, U.; Nenert, G.; Simon, Ch.; Tjia, M. O.; Mostovoy, M.; Palstra, T. T. M. *Phys. Rev. B* **2007**, *75*, 174435.

(28) Adem, U.; Nugroho, A. A.; Meetsma, A.; Palstra, T. T. M. *Phys. Rev. B* **2007**, *75*, 014108.

(29) Asaka, T.; Nemoto, K.; Kimoto, K.; Arima, T.; Matsui, Y. *Phys. Rev. B* **2005**, *71*, 014114.

(30) Mori, S.; Tokunaga, J.; Horibe, Y.; Aikawa, Y.; Katsufuji, T. *Phys. Rev. B* **2005**, *72*, 224434.

(31) Samal, S. L.; Green, W.; Lofland, S. E.; Ramanujachary, K. V.; Das, D.; Ganguli, A. K. *J. Solid State Chem.* **2008**, *181*, 61.

(32) Dixit, A.; Smith, A. E.; Subramanian, M. A.; Lawes, G. *Solid State Commun.* **2010**, *150*, 746.

(33) Zhang, C.; Zhang, X.; Sun, Y.; Liu, S. *Phys. Rev. B* **2011**, *83*, 054104.

(34) Greedan, J. E.; Bieringer, M.; Britten, J. F.; Giaquinta, D. M.; zur Loye, H. C. *J. Solid State Chem.* **1995**, *116*, 118.

(35) Belik, A. A.; Kamba, S.; Nuzhnyy, D.; Tachibana, M.; Takayama-Muromachi, E.; Goian, V. *Phys. Rev. B* **2009**, *79*, 054411.

(36) Serrao, C. R.; Krupanidhi, S. B.; Bhattacharjee, J.; Waghmare, U. V.; Kundu, A. K.; Rao, C. N. R. *J. Appl. Phys.* **2006**, *100*, 076104.

(37) Shannon, R. D.; Prewitt, C. T. *J. Inorg. Nucl. Chem.* **1968**, *30*, 1389.

(38) Moller, A.; Low, U.; Taetz, T.; Kriener, M.; Andre, G.; Damay, F.; Heyer, O.; Braden, M.; Mydosh, J. A. *Phys. Rev. B* **2008**, *78*, 024420.

(39) Nishibori, E.; Takata, M.; Kato, K.; Sakata, M.; Kubota, Y.; Aoyagi, S.; Kuroiwa, Y.; Yamakata, M.; Ikeda, N. *Nucl. Instrum. Methods Phys. Res. Sect. A* **2001**, *467*−*468*, 1045.

(40) Izumi, F.; Ikeda, T. *Mater. Sci. Forum* **2000**, *321*−*324*, 198.

(41) In *International Tables for Crystallography*, 5th ed.; Hahn, T., Ed.; Kluwer: Dordrecht, The Netherlands, 2002; Vol. A, p 52.

(42) Florosa, N.; Rijssenbeeka, J. T.; Martinsona, A. B.; Poeppelmeier, K. R. *Solid State Sci.* **2002**, *4*, 1495.

(43) Mizoguchi, H.; Sleight, A. W.; Subramanian, M. A. *Inorg. Chem.* **2011**, *50*, 10.

(44) Petzelt, J.; Dvořák, V. In *Vibration Spectroscopy of Phase Transitions*; Iqbal, Z., Owens, F. J., Eds.; Academic Press: Orlando, FL, 1984; p 55.

(45) Iliev, M. N.; Lee, H. G.; Popov, V. N.; Abashev, M. V.; Hamed, A.; Meng, R. L.; Chu, C. W. *Phys. Rev. B* **1997**, *56*, 2488.

(46) Smith, A. E.; Sleight, A. W.; Subramanian, M. A. *Mater. Res. Bull.* **2011**, *46*, 1.

(47) Choudhury, D.; Venimadhav, A.; Kakarla, C.; Delaney, K. T.; Devi, P. S.; Mondal, P.; Nirmala, R.; Gopalakrishnan, J.; Spaldin, N. A.; Waghmare, U. V.; Sarma, D. D. *Appl. Phys. Lett.* **2010**, *96*, 162903.

(48) Choudhury, D.; Hazarika, A.; Venimadhav, A.; Kakarla, C.; Delaney, K. T.; Devi, P. S.; Mondal, P.; Nirmala, R.; Gopalakrishnan, J.; Spaldin, N. A.; Waghmare, U. V.; Sarma, D. D. *Phys. Rev. B* **2010**, *82*, 134203.

(49) Oak, M.-A.; Lee, J.-H.; Jang, H. M.; Goh, J. S.; Choi, H. J.; Scott, J. F. *Phys. Rev. Lett.* **2011**, *106*, 047601.

(50) Overton, A. J.; Best, J. L.; Saratovsky, I.; Hayward, M. A. *Chem. Mater.* **2009**, *21*, 4940.

(51) Belik, A. A.; Matsushita, Y.; Tanaka, M.; Takayama-Muromachi, E. *Angew. Chem., Int. Ed.* **2010**, *49*, 7723.

(52) Belik, A. A.; Furubayashi, T.; Matsushita, Y.; Tanaka, M.; Hishita, S.; Takayama-Muromachi, E. *Angew. Chem., Int. Ed.* **2009**, *48*, 6117.

(53) Gelard, I.; Jehanathan, N.; Roussel, H.; Gariglio, S.; Lebedev, O. I.; Van Tendeloo, G.; Dubourdieu, C. *Chem. Mater.* **2011** 10.1021/cm1029358.

(54) Goian, V.; Kamba, S.; Kadlec, C.; Nuzhnyy, D.; Kuzel, P.; Moreira, J. A.; Almeida, A.; Tavares, P. B. *Phase Transitions* **2010**, *83*, 931.